

# NIHAO XVIII: Origin of the MOND phenomenology of galactic rotation curves in a $\Lambda$ CDM universe

Aaron A. Dutton,<sup>1</sup><sup>★</sup> Andrea V. Macciò,<sup>1,2</sup> Aura Obreja,<sup>3,1</sup> Tobias Buck<sup>2</sup>

<sup>1</sup>*New York University Abu Dhabi, PO Box 129188, Abu Dhabi, United Arab Emirates*

<sup>2</sup>*Max-Planck-Institut für Astronomie, Königstuhl 17, 69117 Heidelberg, Germany*

<sup>3</sup>*University Observatory Munich, Scheinerstraße 1, D-81679 Munich, Germany*

20 February 2019

## ABSTRACT

The phenomenological basis for Modified Newtonian Dynamics (MOND) is the radial-acceleration-relation (RAR) between the observed acceleration,  $a = V_{\text{rot}}^2(r)/r$ , and the acceleration accounted for by the observed baryons (stars and cold gas),  $a_{\text{bar}} = V_{\text{bar}}^2(r)/r$ . We show that the RAR arises naturally in the NIHAO sample of 89 high-resolution  $\Lambda$ CDM cosmological galaxy formation simulations. The overall scatter from NIHAO is just 0.079 dex, consistent with observational constraints. However, we show that the scatter depends on stellar mass. At high masses ( $10^9 \lesssim M_{\text{star}} \lesssim 10^{11} M_{\odot}$ ) the simulated scatter is just  $\approx 0.04$  dex, increasing to  $\approx 0.11$  dex at low masses ( $10^7 \lesssim M_{\text{star}} \lesssim 10^9 M_{\odot}$ ). Observations show a similar dependence for the intrinsic scatter. At high masses the intrinsic scatter is consistent with the zero scatter assumed by MOND, but at low masses the intrinsic scatter is non-zero, strongly disfavoring MOND. Applying MOND to our simulations yields remarkably good fits to most of the circular velocity profiles. In cases of mild disagreement the stellar mass-to-light ratio and/or “distance” can be tuned to yield acceptable fits, as is often done in observational mass models. In dwarf galaxies with  $M_{\text{star}} \sim 10^6 M_{\odot}$  MOND breaks down, predicting lower accelerations than observed and in our  $\Lambda$ CDM simulations. The assumptions that MOND is based on (e.g., asymptotically flat rotation curves, zero intrinsic scatter in the RAR) are only approximately true in  $\Lambda$ CDM. Thus if one wishes to go beyond Newtonian dynamics there is more freedom in the observed RAR than assumed by MOND.

**Key words:** methods: numerical – galaxies: fundamental parameters – galaxies: haloes – galaxies: kinematics and dynamics – dark matter

## 1 INTRODUCTION

The observational evidence for dark matter goes back many decades. Zwicky (1933) showed that if the Virgo cluster is bound, its total mass must greatly exceed the sum of the masses of the individual members. In the 1970’s galaxy rotation curves were found to level off at large radii, implying the presence of substantial mass outside the optically visible dimensions of galaxies (Faber & Gallagher 1979).

Further evidence for missing mass comes from the growth of cosmic structure. The Cosmic Microwave Background (CMB) is remarkably uniform with temperature fluctuations  $\Delta T/T = \Delta\rho/\rho \sim 10^{-5}$  (Smoot et al. 1992). In order for these density fluctuations to grow into the observed galaxies  $\Delta\rho/\rho \sim 10^6$ , they need to increase by a factor of  $10^{11}$ ! In the baryon-dominated universe, in order to have nonlinear

structure now, the induced fluctuations in the CMB would have to be much larger than is observed. In a dark matter dominated universe, dark matter perturbations grow prior to recombination, and this induces a rapid growth in baryon perturbations shortly after recombination, allowing nonlinear structure to form now from a smaller baryon fluctuation at recombination (Bond et al. 1980).

An alternative to dark matter was proposed by Milgrom (1983) who considered the possibility that rather than there being missing mass in galaxies, there is modification to Newtonian dynamics (MOND) at low accelerations  $a < a_0$ , where  $a_0 \sim 10^{-10} \text{ m s}^{-2}$ . The observed centripetal acceleration (in the plane of the disk) is defined as

$$a(r) = V^2(r)/r = -\partial\Phi(r)/\partial r, \quad (1)$$

where  $\Phi$  is the total gravitational potential. Likewise, the acceleration predicted due to the observed baryons,  $a_{\text{bar}} =$

★ dutton@nyu.edu

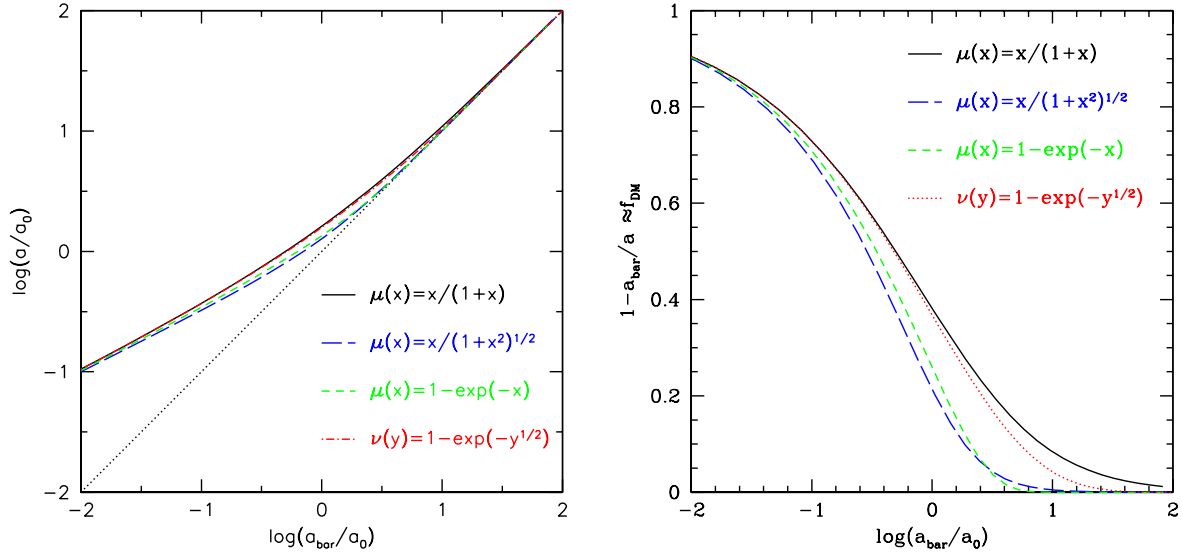


**Figure 1.** Commonly used MOND interpolation functions of the form  $a\mu(a/a_0) = a_{\text{bar}}$ , and  $a = a_{\text{bar}}/\nu(a_{\text{bar}}/a_0)$ . Left:  $a$  vs  $a_{\text{bar}}$  on a log-scale (radial acceleration relation), right:  $1 - a_{\text{bar}}/a \approx f_{\text{DM}}$  vs  $a_{\text{bar}}$  (mass discrepancy - acceleration relation) with a linear vertical scale to highlight the differences between fitting functions. The dotted line shows the 1:1 relation.

$V_{\text{bar}}^2/r$ . The following assumptions restrict the form of the modification to Newtonian dynamics.

**Assumption 1:** there is no missing mass at high accelerations. Thus

$$a(r) = a_{\text{bar}}(r), \quad (a \gg a_0). \quad (2)$$

**Assumption 2:** rotation curves are asymptotically flat at low accelerations. At large radii the total acceleration is given by  $a(r) = V_{\text{flat}}^2/r$ , and the enclosed baryonic mass is a constant:  $a_{\text{bar}}(r) = V_{\text{bar}}^2(r)/r = GM_{\text{bar}}/r^2$ . Requiring that  $a$  is a function of  $a_{\text{bar}}$  and not radius implies

$$V_{\text{flat}}^4 = GM_{\text{bar}}a^2/a_{\text{bar}}. \quad (3)$$

Since  $V_{\text{flat}}$ ,  $G$ , and  $M_{\text{bar}}$  are constants, this implies

$$a^2(r)/a_{\text{bar}}(r) \equiv a_0, \quad (a \ll a_0) \quad (4)$$

is also a constant. Note that Eq. 3 is a Baryonic Tully-Fisher relation with slope of 4.

**Assumption 3:** there is a unique interpolation function,  $\mu(x)$ , between the two acceleration extremes:

$$a(r)\mu(a/a_0) = a_{\text{bar}}(r). \quad (5)$$

However, this interpolation function is not specified by the theory. A popular choice is

$$\mu(x) = x/\sqrt{1+x^2}. \quad (6)$$

This can be inverted to express  $a$  in terms of  $a_{\text{bar}}$  (van den Bosch & Dalcanton 2000):

$$a(r) = a_{\text{bar}}(r) \left( \frac{1}{2} + \frac{1}{2} \sqrt{1 + 4a_0^2/a_{\text{bar}}^2} \right)^{1/2}. \quad (7)$$

Other choices and their inversions include

$$\mu(x) = x/(1+x); \quad (8)$$

$$a(r) = a_{\text{bar}}(r) \left( \frac{1}{2} + \frac{1}{2} \sqrt{1 + 4a_0/a_{\text{bar}}} \right), \quad (9)$$

and

$$\mu(x) = 1 - \exp(-x); \quad (10)$$

Alternatively McGaugh et al. (2016) adopt

$$a(r) = a_{\text{bar}}(r)/\nu(a_{\text{bar}}/a_0) \quad (11)$$

with

$$\nu(y) = (1 - \exp(-\sqrt{y})) \quad (12)$$

and find  $a_0 = 1.20 \pm 0.02(\text{ran.}) \pm 0.24(\text{sys.}) \times 10^{-10} \text{ m s}^{-2}$ .

Fig. 1 shows these interpolation functions. On a logarithmic scale over 4 orders of magnitude the differences appear small (left panel). Upon closer inspection the differences are significant (right panel). At  $a_{\text{bar}} = a_0$  the mass discrepancy expressed as the dark matter fraction varies from  $0.2 \lesssim f_{\text{DM}} \lesssim 0.4$ . At  $a_{\text{bar}} = 10a_0$ , the mass discrepancy varies from  $0.0 \lesssim f_{\text{DM}} \lesssim 0.1$ . These differences highlight the non-uniqueness of predictions from MOND. The relation between total acceleration and baryonic acceleration (left panel) is often referred to as the radial acceleration relation (RAR), while the relation between the mass discrepancy and baryonic acceleration (right panel) is often referred to as the mass discrepancy acceleration relation (MDAR, Sanders 1990; McGaugh 2004).

There have been numerous theoretical studies of the RAR in a  $\Lambda$ CDM context, using both analytic models and cosmological hydrodynamical simulations (e.g., van den Bosch & Dalcanton 2000; Di Cintio & Lelli 2016; Desmond 2017; Keller & Wadsley 2017; Ludlow et al. 2017; Navarro et al. 2017). These authors have shown that galaxy formation in a  $\Lambda$ CDM universe results in a RAR close to, but not identically equal to that commonly ascribed to MOND.

In this paper we use the NIHAO suite of cosmological galaxy formation simulations (Wang et al. 2015) to gain insight into the origin of the RAR in a  $\Lambda$ CDM universe. Compared to previous cosmological hydrodynamical simulations, NIHAO has more galaxies with higher resolution over a wider range of galaxy stellar masses  $10^5 \lesssim M_{\text{star}} \lesssim 10^{11} M_{\odot}$ . In §2 we describe the observations we compare to from the SPARC survey (Lelli et al. 2016). In §3 we describe the NIHAO galaxy simulations. In §4 we present the RAR from NIHAO and compare to observations from SPARC. In §5 we investigate the origin of the small scatter in the RAR, and present a comparison of dark matter profiles. We finish with a summary in §6.

## 2 SPARC OBSERVATIONS

As our observational sample we use the Spitzer Photometry and Accurate Rotation Curves (SPARC) database (Lelli et al. 2016). SPARC is the largest sample of galaxy rotation curves with spatially resolved data on the distribution of both stars and gas. The full sample of 175 galaxies spans the full range of stellar masses of rotationally supported galaxies ( $10^7 \lesssim M_{\text{star}} \lesssim 10^{11} M_{\odot}$ ). It includes near-infrared ( $3.6\mu\text{m}$ ) observations to trace the distribution of stellar mass and 21 cm observations that trace the atomic hydrogen gas (HI). The 21 cm data also provide velocity fields from which rotation curves are derived. In some cases the rotation curves are supplemented with higher spatial resolution rotation curves from ionized gas. All rotation curves are nominally corrected for inclination.

Following McGaugh et al. (2016) we apply some quality criteria. Ten galaxies with inclination  $i < 30$  are removed to minimize  $\sin(i)$  corrections to the observed velocities. Twelve galaxies with asymmetric rotation curves are rejected (these are flagged with  $Q = 3$ ). This leaves a sample of 153 galaxies. Additionally, only data points with relative velocity errors less than 10% are kept.

Fig. 2 shows histograms of the global stellar and atomic hydrogen gas properties of the SPARC galaxies (blue lines), and NIHAO simulations (red shaded, see §3): Stellar mass,  $M_{\text{star}}$ ; half-light radius at 3.6 micron,  $R_{\text{star}}$ ; atomic hydrogen mass,  $M_{\text{HI}}$ ; and radius at which HI density equals 1 [ $M_{\odot} \text{pc}^{-2}$ ],  $R_{\text{HI}}$ . The upper left panel of Fig. 3 shows the rotation curves of this sample, where the color code corresponds to the stellar mass. The boundaries of the mass bins are  $\log(M_{\text{star}}/M_{\odot}) = 6.7, 8.0, 9.3, 10.2, 11.4$ . The lower panel shows average rotation curves in bins of stellar mass. For each mass bin we interpolate each rotation curve onto a radial grid, then we average in  $\log(V)$ . We also calculate the average minimum and maximum radius, which defines the range over which the average rotation curves are plotted. The mean mass is given to the right of each average rotation curve. We see the shape and extent of the rotation curve systematically changes from low to high mass.

Here we briefly discuss uncertainties in the observations.

(i) Conversion from stellar light to stellar mass. The nominal value is assumed to be  $M/L_{3.6} = 0.5$  for the disk and 0.7 for the bulge (McGaugh et al. 2016), but could plausibly vary from 0.2 to 1.0 depending on initial mass function (IMF), age and metallicity (McGaugh & Schombert 2015).

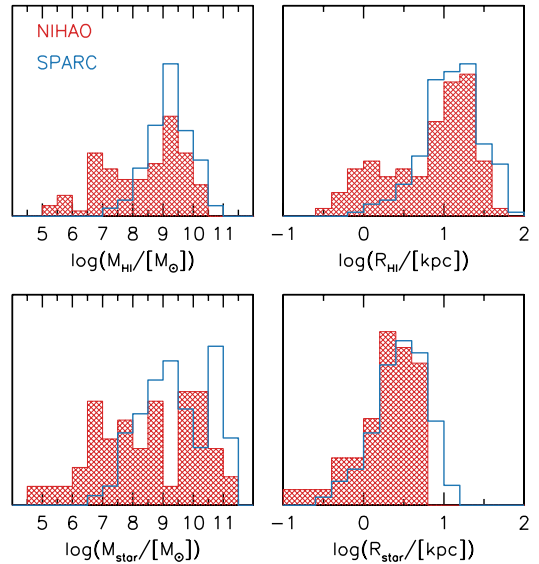


**Figure 2.** Histograms of masses and sizes for atomic hydrogen and stars from NIHAO simulations (red, shaded), and SPARC observations (blue). For SPARC the stellar masses and projected half-light radii are obtained from  $3.6\mu\text{m}$  photometry, while for NIHAO they are calculated from the stellar particles.

(ii) Distance. Since these galaxies are nearby, distance errors can be significant (up to 30%). Only a subset of the SPARC sample has accurate (5%) distances from e.g., using the Tip of the Red Giant Branch (TRGB). Since physical size scales as  $D$ , and luminosity as  $D^2$ , the acceleration of the baryons ( $\sim M_{\text{bar}}/r^2$ ) is independent of distance. The observed rotation velocity is also independent of distance (ignoring beam smearing which is worse for more distant galaxies), so that the total acceleration depends on distance as  $D^{-1}$ .

(iii) Rotation curves. The conversion from observed rotation to circular velocity depends on inclination, pressure support and warps (especially at large radii).

(iv) Gas budget. The majority of gas in the galaxy is in atomic hydrogen, which is observed for SPARC galaxies, but there is also a small amount of molecular and ionized gas, which is not easily observed, and generally missing from the SPARC data.

## 3 NIHAO GALAXY FORMATION SIMULATIONS

For theoretical predictions for the RAR in a  $\Lambda$ CDM universe we use the NIHAO galaxy formation simulations (Wang et al. 2015). These are a sample of  $\sim 90$  cosmological hydrodynamical galaxy formation simulations run with the SPH code GASOLINE2 (Wadsley et al. 2017).

Haloes are selected at redshift  $z = 0$  from parent dissipationless simulations of size 60, 20, & 15  $\text{Mpc}/h$ , presented in Dutton & Macciò (2014) which adopt a flat  $\Lambda$ CDM cosmology with parameters from the Planck Collaboration et al. (2014): Hubble parameter  $H_0 = 67.1 \text{ km s}^{-1} \text{ Mpc}^{-1}$ , matter density  $\Omega_m = 0.3175$ , dark energy density  $\Omega_\Lambda = 1 - \Omega_m =$

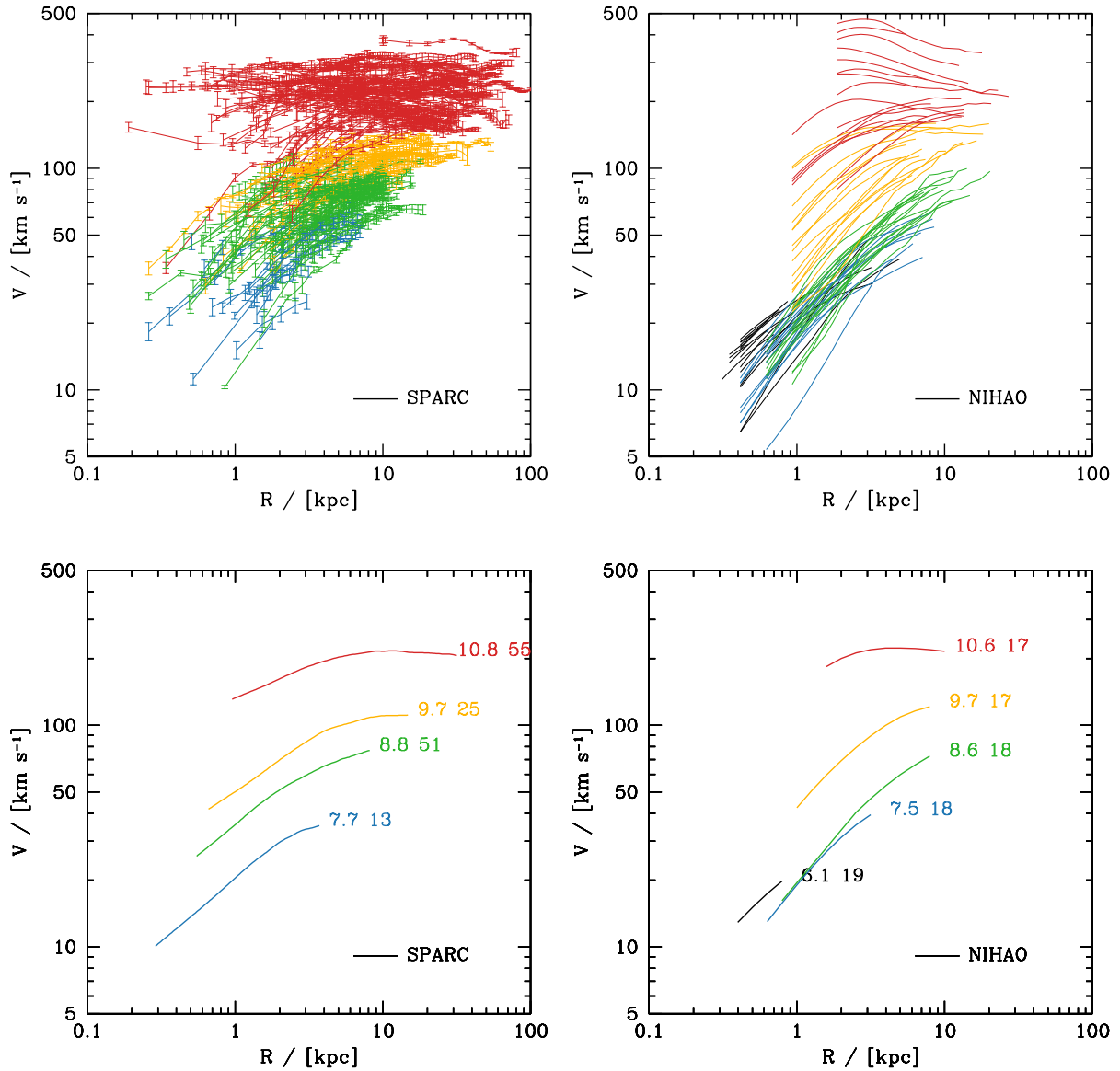


**Figure 3.** Rotation curves from SPARC observations (left) and circular velocity profiles in the plane of the disk from NIHAO simulations (right). Upper panels show all the individual profiles color coded by the stellar mass. The boundaries of the mass bins are  $\log(M_{\text{star}}/M_{\odot}) = 4.5, 7.0, 8.0, 9.3, 10.2, 11.4$ , and are chosen to have equal numbers of simulated galaxies in each bin. For NIHAO these are shown from twice the force softening of the dark matter particles to the HI radius (which encloses 90% of the HI mass). Lower panels show mean profiles in bins of stellar mass, and are plotted between the average minimum and maximum radii of the profiles. The mean stellar masses are shown to the right of each line (this can be slightly different between NIHAO and SPARC due to the different distribution of galaxies within each mass bin).

0.6825, baryon density  $\Omega_b = 0.0490$ , power spectrum normalization  $\sigma_8 = 0.8344$ , power spectrum slope  $n = 0.9624$ . Haloes are selected uniformly in log halo mass from  $\sim 10$  to  $\sim 12$  *without* reference to the halo merger history, concentration or spin parameter. Star formation and feedback is implemented as described in [Stinson et al. \(2006, 2013\)](#). Mass and force softening are chosen to resolve the mass profile of the target halo at  $\lesssim 1\%$  the virial radius, which results in  $\sim 10^6$  dark matter particles inside the virial radius of all haloes at  $z = 0$ . The motivation of this choice is to ensure that the simulations resolve the galaxy dynamics on the scale

of the half-light radii, which are typically  $\sim 1.5\%$  of the virial radius ([Kravtsov 2013](#)).

Each hydro simulation has a corresponding dark matter only (DMO) simulation of the same resolution. These simulations have been started using the identical initial conditions, replacing baryonic particles with dark matter particles. The full sample of hydro simulations we use is 89. When comparing hydro to DMO we remove 5 simulations for which either the hydro or DMO simulation is undergoing a major merger and is thus out of equilibrium.

Haloes in NIHAO zoom-in simulations were identified

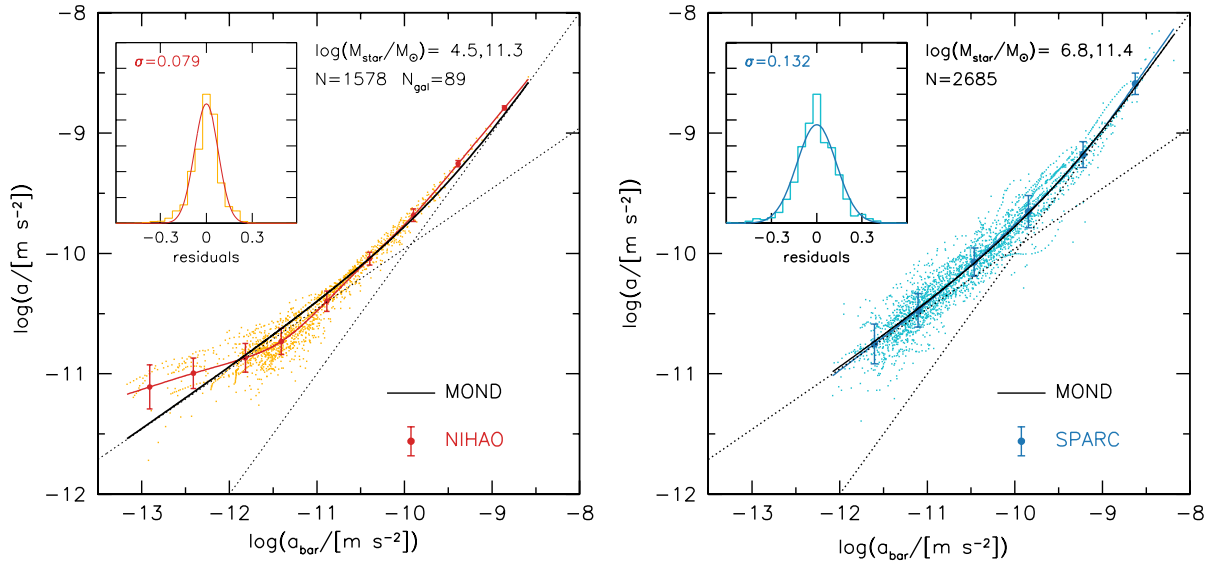


**Figure 4.** Total acceleration,  $a$ , vs acceleration due to baryons,  $a_{\text{bar}}$ , in NIHAO simulations (left red/orange) and SPARC observations (right, blue/cyan) compared to MOND (black solid line) with an acceleration scale  $a_0 = 1.2 \times 10^{-10} \text{ m s}^{-2}$ . Small points show the individual data points. Large circles with error bars show the mean and  $1\sigma$  scatter in bins of  $a_{\text{bar}}$ . The lines show the spline interpolated mean relations. The inset panel shows the residuals (orange/cyan histogram) relative to the interpolated mean relations, which has a standard deviation of just 0.079 dex in NIHAO and 0.132 dex in SPARC. The corresponding Gaussian is shown in red (for NIHAO) and blue (for SPARC). The range of galaxy stellar masses,  $M_{\text{star}}$ , is as indicated, while  $N$  is the number of data points.

using the MPI+OpenMP hybrid halo finder AHF<sup>1</sup> (Gill et al. 2004; Knollmann & Knebe 2009). AHF locates local overdensities in an adaptively smoothed density field as prospective halo centers. In this study we use one halo from each zoom-in simulation (the one with the most particles). The virial masses of the haloes are defined as the masses within a sphere whose average density is 200 times the cosmic critical matter density,  $\rho_{\text{crit}} = 3H_0^2/8\pi G$ . The virial mass, size and circular velocity of the hydro simulations are denoted:  $M_{200}$ ,  $R_{200}$ ,  $V_{200}$ . The corresponding properties for the dark matter only simulations are denoted with a superscript, DMO. For the baryons we calculate masses enclosed within spheres of radius  $r_{\text{gal}} = 0.2R_{200}$ , which corresponds to  $\sim 10$  to  $\sim 50$  kpc. The stellar mass inside  $r_{\text{gal}}$  is  $M_{\text{star}}$ , the atomic hydrogen, HI, inside  $r_{\text{gal}}$  is computed following Rahmati et al. (2013) as described in Gutcke et al. (2017).

The NIHAO simulations are the largest set of cosmological zoom-ins covering the halo mass range  $10^{10} \lesssim M_{200} \lesssim 10^{12} M_{\odot}$ . Their uniqueness is in the combination of high spatial resolution coupled to a statistical sample of haloes. In the context of  $\Lambda$ CDM they form the “right” amount of stars both today and at earlier times (Wang et al. 2015). Their cold gas masses and sizes are consistent with observations (Stinson et al. 2015; Macciò et al. 2016; Dutton et al. 2019), they follow the gas, stellar, and baryonic Tully-Fisher relations (Dutton et al. 2017). On the scale of dwarf galaxies the dark matter haloes expand yielding cored dark matter density profiles consistent with observations (Tollet et al. 2016), and resolve the too-big-to-fail problem of field galaxies (Dutton et al. 2016). They reproduce the diversity of dwarf

galaxy rotation curve shapes Santos-Santos et al. (2018), and the HI linewidth velocity function (Macciò et al. 2016; Dutton et al. 2019). They match the observed clumpy morphology of galaxies seen in CANDELS (Buck et al. 2017). As such they provide a good template with which to study the RAR in a  $\Lambda$ CDM context.

Histograms of the stellar and atomic hydrogen masses and sizes are shown with red shading in Fig. 2. Broadly speaking NIHAO and SPARC have similar distributions, but NIHAO extends to lower masses. The right panels of Fig. 3 shows the circular velocity profiles from the NIHAO galaxy formation simulations. These have been calculated using the potential in the plane of the disk using Eq.1. The NIHAO simulations have been plotted from two dark matter force softening lengths ( $\approx$  the convergence radius), to the radius enclosing 90% of the HI ( $\approx$  the edge of the observable galactic HI). The radial range of the velocity profiles is similar, but slightly narrower. The change in velocity profile shapes from low to high mass is similar between simulations and observations. In detail there are differences, caused at least in part by differences in the distribution of baryons.

#### 4 THE RADIAL ACCELERATION RELATION

Fig. 4 shows the relation between total acceleration,  $a$ , and the acceleration due to the baryons,  $a_{\text{bar}}$  for NIHAO galaxies (left) and SPARC observations (right). The dots show all of the individual measurements for observed and simulated galaxies. The total number of data points,  $N \sim 1400$  for NIHAO and  $N \sim 2700$  for SPARC. For NIHAO we sample the circular velocity profiles linearly in units of the virial radius, but we only include points which are observable (i.e.,

<sup>1</sup> <http://popia.ft.uam.es/AMIGA>

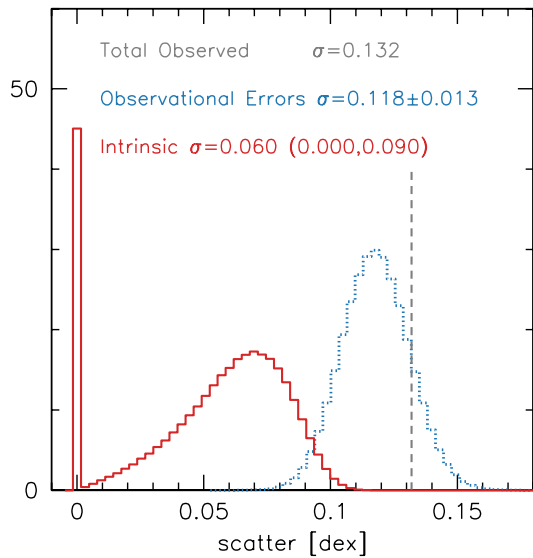


**Figure 5.** Scatter in the RAR. The total observed scatter is 0.132 (grey dashed vertical line). The observational errors contribute  $0.118 \pm 0.013$  (blue dotted histogram). Subtracting the observational errors gives the intrinsic scatter (red histogram). For cases where the observed error is greater than the total scatter we set  $\sigma = 0$ , which is the spike. The intrinsic scatter has a median of 0.06 and a 90% confidence interval of 0.00 to 0.09.

within the HI radius). This is similar to the observations, which tend to sample the rotation curves linearly in radius, and with similar numbers of data points for different mass galaxies. The large points with error bars show the mean of  $\log_{10}(a)$  in bins of  $\log_{10}(a_{\text{bar}})$ , while the error bar shows the scatter about the spline interpolated mean relation.

The solid black line shows the relation fitted to SPARC data by [McGaugh et al. \(2016\)](#). The functional form was chosen to follow the asymptotic relations for high and low accelerations in MOND (dotted lines). Overall the NIHAO simulations provide a very good match to the observed RAR. The agreement is especially good when one considers that there are observational systematics, such as the stellar mass-to-light ratio and distance scale that can shift the observed relation ([McGaugh et al. 2016](#); [Lelli et al. 2017](#)). Furthermore, the NIHAO simulations are necessarily an approximation for how galaxies form in a  $\Lambda$ CDM universe.

The inset panels show the scatter about the interpolated mean relation (histogram). The standard deviation and corresponding Gaussian is given in red (for NIHAO) and blue (for SPARC). The scatter from NIHAO is just 0.079 dex. Similar small scatters were reported by other  $\Lambda$ CDM simulation studies ([Keller & Wadsley 2017](#); [Ludlow et al. 2017](#)). This is less than the total observed scatter of 0.132 dex. However, there are observational errors which means the intrinsic scatter is lower. Note one should be aware that in principle observational errors can correlate with offsets from the RAR leading to lower observed than intrinsic scatter. For example if galaxies with higher stellar  $M/L$  have lower  $a$ , this would result in the RAR measured with constant  $M/L$  having less scatter than the true RAR.

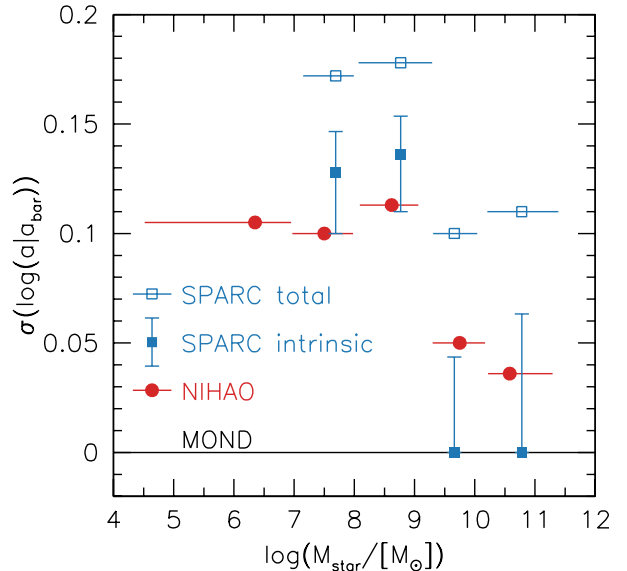


**Figure 6.** Mass dependence of scatter in the RAR. Red circles show results from NIHAO simulations. Blue squares show the total and intrinsic scatter from SPARC galaxies. The vertical error bars show the intrinsic scatter from SPARC adopting measurement errors of 0.09 and 0.14 dex, for the upper and lower limit, respectively. The horizontal lines show the range of  $M_{\text{star}}$  in each bin.

#### 4.1 Intrinsic scatter from observations

As discussed above, observational sources of error include distance, stellar mass-to-light ratio, disk inclination, rotation velocity, and atomic hydrogen flux. According to [McGaugh et al. \(2016\)](#) these contribute 0.08, 0.06, 0.05, 0.03, 0.01 dex to the scatter in  $a$  at  $a_{\text{bar}}$ , yielding a total observational error of 0.116 dex. Subtracting this (in quadrature) from the total observed scatter of 0.132 dex yields an intrinsic scatter of 0.063 dex.

However, it should be noted that the observational errors are just estimates. The true observational errors could be larger or smaller. For example, [McGaugh et al. \(2016\)](#) adopt an error on the stellar mass-to-light ratio of 0.11 dex. The true error could plausibly be anywhere in the range 0.05 to 0.20 dex, and it could depend systematically on the galaxy mass, or other galaxy property. To get an idea of the plausible range of the intrinsic scatter we assume the observational errors are drawn from a Gaussian with the mean specified above, and a standard deviation of 20% of the mean. For example, if the distance errors are reported to be 0.08 dex, we adopt a standard deviation of 0.016 dex.

Assuming the uncertainties in the errors of the five sources are uncorrelated, using a Monte Carlo simulation the total observational error is  $0.118 \pm 0.013$  (Fig. 5). Subtracting this from the total observed scatter of 0.132 dex yields an intrinsic scatter with a wide variation (red histogram). The 90% confidence interval ranges from zero to 0.090 dex. Thus the scatter in the RAR from our simulations of 0.079 dex is consistent with the observations. The prediction from MOND for zero intrinsic scatter is also consistent with the observations. In order to use the scatter in the RAR to distinguish between  $\Lambda$ CDM and MOND, either a more accurate

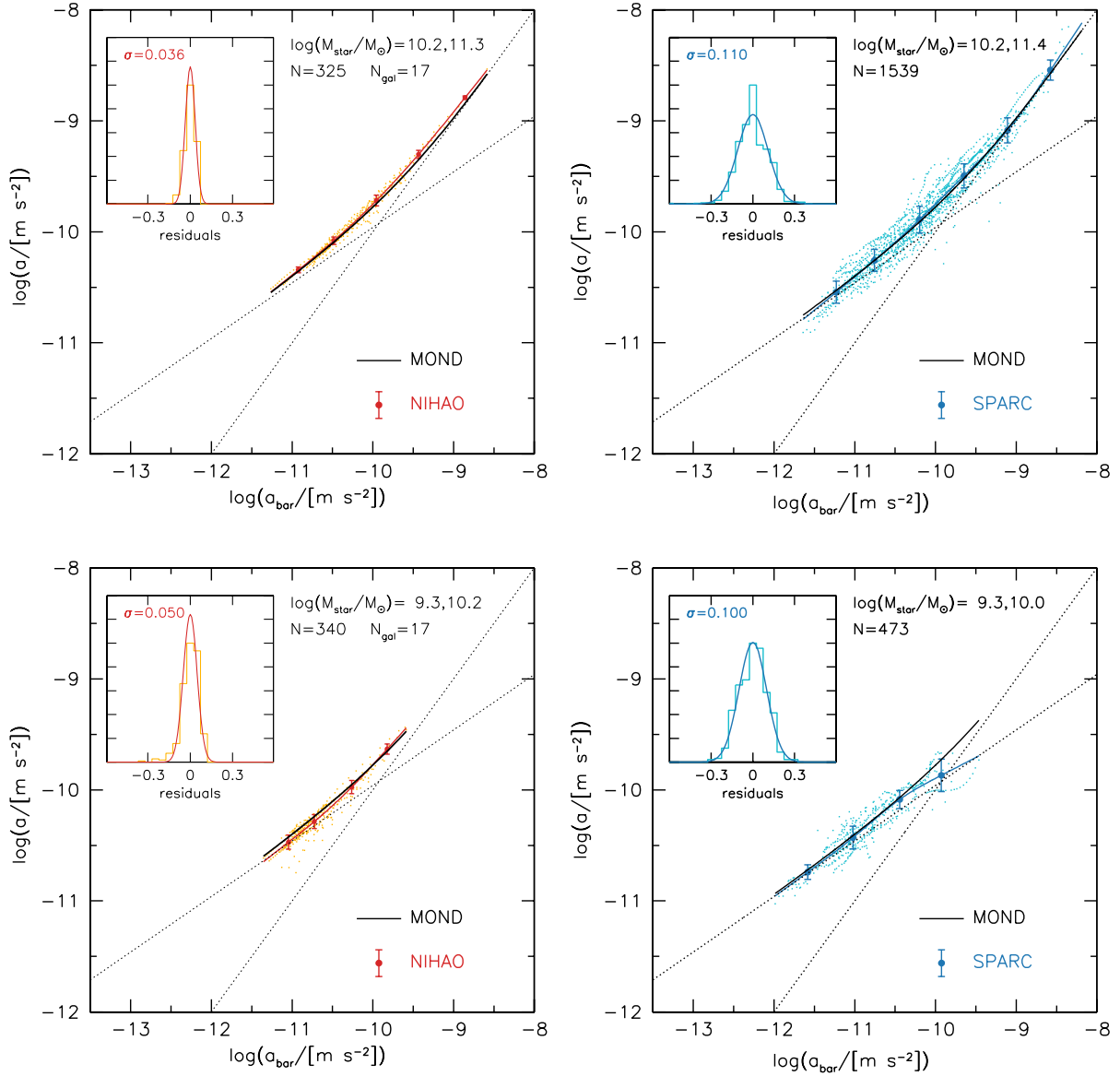


**Figure 7.** As Fig. 4 but for galaxies in narrow stellar mass ranges as indicated at the top right of each panel. At these (high) masses the simulated RAR is very similar to the observed one, and has very small scatter making the individual data points are hard to see.

measurement is required, or as we shall see below we need to look at the RAR scatter for different mass galaxies.

The largest source of observational uncertainty are the distances, which account for half of the total variance. So if these can be reduced a significant improvement in the intrinsic scatter is possible. The galaxies with the largest distance errors from the SPARC survey use the Hubble flow,  $D = v_{\text{sys}}/H_0$ , so the unknown peculiar velocities provide a random source of error, while the value of the Hubble constant provides a systematic error. The peculiar velocity error can be reduced by simply observing galaxies at larger distances. This is easier said than done, because galaxies that are further away have smaller angular sizes. It is possible to obtain rotation curves using optical emission lines for such galaxies (e.g., Courteau et al. 2007), but atomic hydrogen gas maps will require future radio telescopes such as the

Square Kilometer Array (SKA). These will have the resolution and sensitivity to measure HI density maps and rotation curves of galaxies at large enough distances such that peculiar velocity errors are negligible.

#### 4.2 Mass dependence of the RAR

The dependence of the scatter in the RAR on stellar mass is shown in Fig. 6. In both simulations and observations higher mass galaxies have smaller scatter than lower mass galaxies. In the highest mass bin centered on  $M_{\text{star}} \approx 10^{10.7} M_{\odot}$ , the scatter in NIHAO is just 0.036 dex (0.045 dex relative to MOND), compared with 0.110 dex for SPARC. In the mass bin centered on  $M_{\text{star}} \approx 10^{7.5} M_{\odot}$  the scatter in NIHAO increases to 0.10 dex (0.14 dex relative to MOND), compared with 0.172 dex for SPARC.

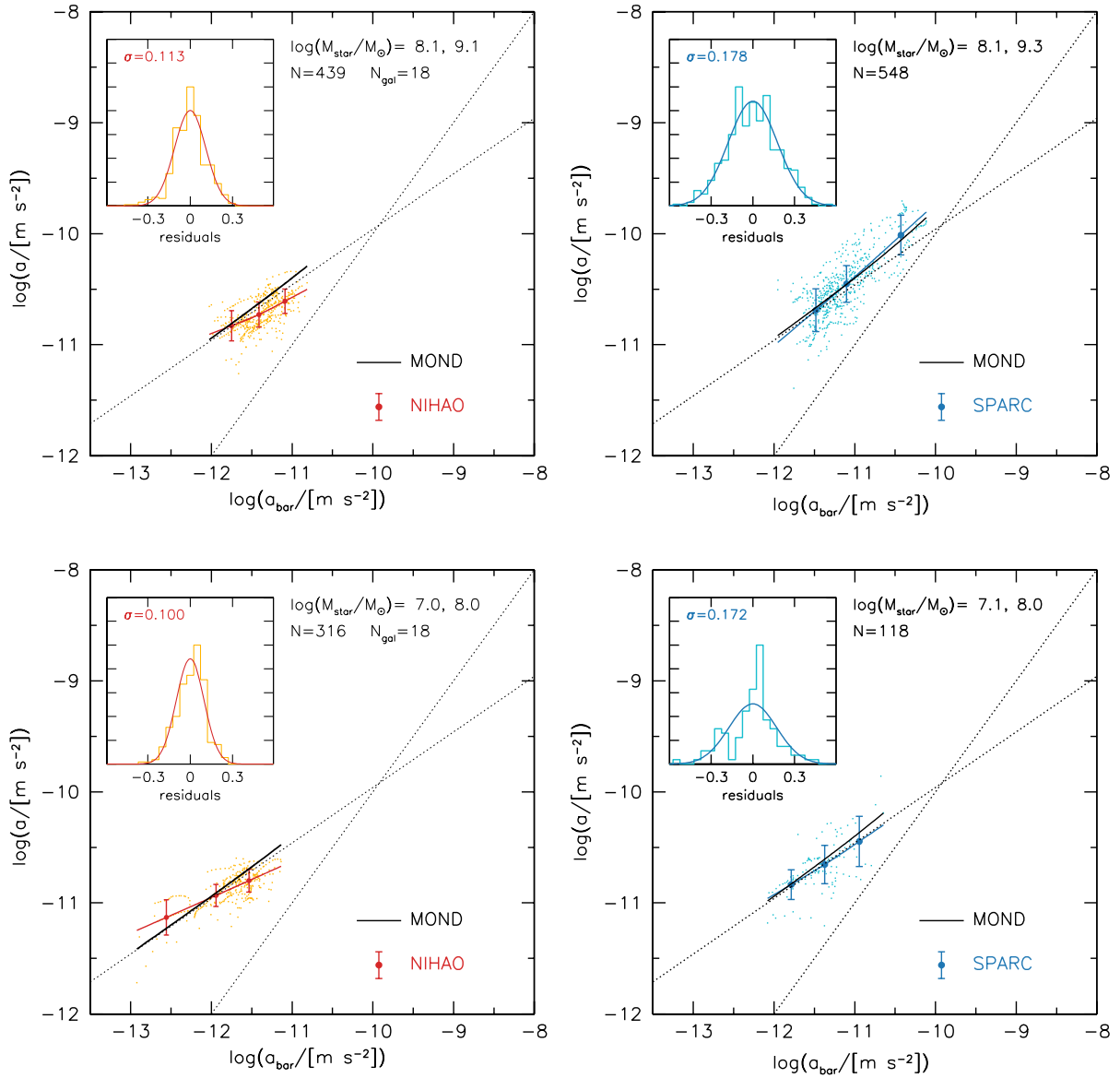


**Figure 8.** As Fig. 4 but for galaxies in narrow stellar mass ranges as indicated at the top right of each panel. At these (low) masses the simulated RAR shows small but significant deviations from the observed one. Both simulations and observations have larger scatter than at higher masses.

The quadratic differences between the simulated and observed scatter from high to low mass are 0.104, 0.087, 0.138, and 0.140 dex. In other words, these are the size of the measurement errors needed to reconcile the observed scatter with the simulated scatter. Based on Fig. 5 and the reported measurement errors for SPARC galaxies, which do not vary significantly with galaxy mass, these are reasonable numbers. So we conclude that the mass dependent scatter in the NIHAO RAR is consistent with the intrinsic scatter from observations. The zero scatter assumed by MOND is also consistent with the high mass galaxies  $10^{9.3} \lesssim M_{\text{star}} \lesssim 10^{11.4} M_{\odot}$ , but inconsistent with the low mass galaxies  $10^{7.0} \lesssim M_{\text{star}} \lesssim 10^{9.3} M_{\odot}$ . Thus using the same data that has been used as evidence in favor of MOND by [McGaugh et al. \(2016\)](#), we have shown that the intrinsic

scatter in the RAR actually disfavors MOND, and is in excellent agreement with predictions from  $\Lambda$ CDM. Our result echos that of [Rodrigues et al. \(2018\)](#) who concluded that the observed rotation curves from SPARC could not be fitted with MOND assuming a universal value of the acceleration scale,  $a_0$ .

Figs. 7 & 8 shows the RAR divided into four bins of stellar mass centered on  $M_{\text{star}} \approx 10^{7.5}$ ,  $10^{8.8}$ ,  $10^{10.0}$ , and  $10^{10.9} M_{\odot}$ . These bins are the same as used in Fig. 3, and have been chosen to have roughly the same number of NIHAO galaxies per bin.

A feature that stands out in both simulations and observations is that higher mass galaxies span a wider range of accelerations than lower mass galaxies. This is due to the systematic change in the shape of the circular velocity pro-



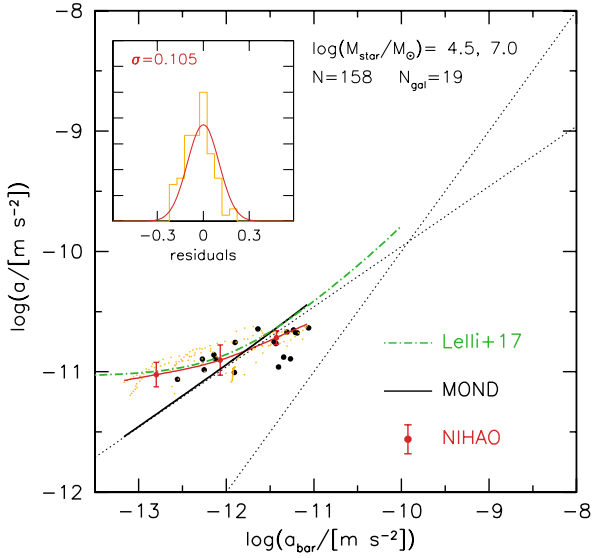


**Figure 9.** Total acceleration,  $a$ , vs acceleration due to baryons,  $a_{\text{bar}}$ , for the lowest stellar mass galaxies in NIHAO. Black circles show the acceleration at the projected stellar half-mass radii. These galaxies deviate significantly from the MOND RAR, but are consistent with the observed relation for dwarf spheroidal galaxies (green line, Lelli et al. 2017).

files with galaxy mass (see Fig. 3). The highest mass galaxies have velocity profiles close to constant, and thus acceleration varies inversely with radius, whereas low mass galaxies have rising velocity profiles with slopes close to 0.5, which results in acceleration independent of radius.

For the two highest mass bins  $10^{9.3} \lesssim M_{\text{star}} \lesssim 10^{11.3} M_{\odot}$  (Fig. 7) the mean NIHAO RAR follows the MOND RAR extremely closely. For the two lowest mass bins  $10^{7.0} \lesssim M_{\text{star}} \lesssim 10^{9.3} M_{\odot}$  (Fig. 8) the mean NIHAO RAR shows departures from the MOND RAR. At baryon accelerations of  $a_{\text{bar}} \sim 10^{-11} \text{ ms}^{-2}$  MOND over-predicts NIHAO, while at  $a_{\text{bar}} \lesssim 10^{-12} \text{ ms}^{-2}$  MOND under-predicts NIHAO. This trend continues when we look at even lower mass galaxies.

Fig. 9 shows the RAR for the lowest mass galaxies in NIHAO, with stellar masses between  $10^{4.5} M_{\odot}$  and  $10^{7.0} M_{\odot}$ . These galaxies deviate significantly from the MOND relation below an acceleration scale of  $a_{\text{bar}} = 10^{-12} \text{ m s}^{-2}$ . The green line shows a fit to the observed RAR for dwarf spheroidal galaxies from Lelli et al. (2017). While the observed and simulated dwarfs have similar ranges of stellar masses, there are some differences that should be considered. The observations are primarily satellite galaxies, whereas the simulations are all centrals. The observed total accelerations are based on stellar kinematics, whereas for the simulations we show points sampled from the radii observable with atomic hydrogen (using the same procedure as for more massive galaxies). The black circles in Fig. 9 show the RAR for NIHAO galaxies at the location of the projected half-mass radii of the stars. These points tend to sample higher accelerations, but follow the same trend as the full velocity curve points. Even though there are some caveats in the comparison between our  $\Lambda$ CDM based simulations and observations, the agreement is an encouraging sign.

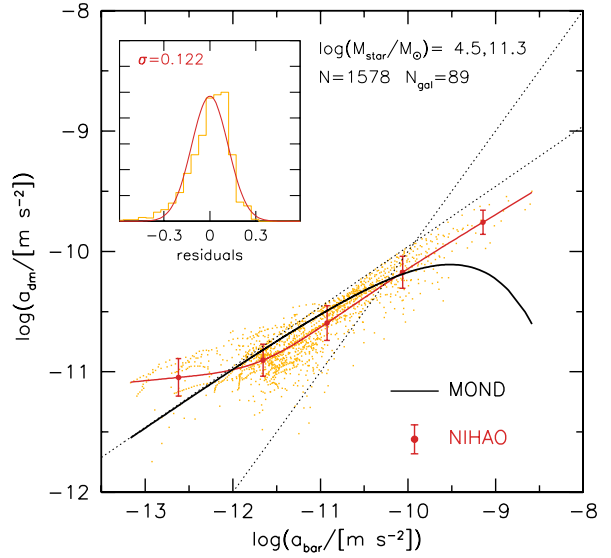


**Figure 10.** Dark matter acceleration,  $a_{\text{dm}}$ , vs acceleration due to baryons,  $a_{\text{bar}}$ , for NIHAO. The points with lowest and highest accelerations deviate the most from the MOND RAR (black line). The dotted lines show the 1:1 relation and the asymptotic MOND relation at low  $a_{\text{bar}}$ .

The deviation of the observed RAR for dwarf Spheroidal galaxies from the MOND prediction is another apparent failure of MOND. The particular assumption that breaks is that the RAR has a slope of 1/2 at low baryon accelerations. Recall, that this assumption was made to ensure that rotation curves are asymptotically flat at large radii.

### 4.3 Other radial acceleration relations

Observationally the two axes of the RAR are independent, however in simulations the two axes are correlated when the dark matter fraction is low, because  $a \equiv a_{\text{bar}} + a_{\text{dm}}$ . Fig. 10 shows an alternative way to look at the RAR: the dark matter acceleration vs the baryon acceleration. This is exactly the same data as in Fig. 4, but with independent axes we clearly see that NIHAO and MOND diverge at high baryon accelerations. The scatter in  $a_{\text{dm}}|a_{\text{bar}}$  is also larger than that of  $a|a_{\text{bar}}$ : 0.122 vs 0.079. Observationally it is not advised to calculate the dark matter acceleration, as measurement errors can result in negative values. However, it would be possible to determine the scatter in  $a_{\text{dm}}$  by forward modelling the observed RAR.

## 5 ORIGIN OF RAR SCATTER IN LCDM

Having established that the NIHAO simulations reproduce the slopes, normalization, and small scatter in the RAR, we now ask: where does the small scatter come from in our simulations?

Since the RAR is a prescription for how the total acceleration is related to the acceleration due to baryons, we can apply the RAR to our simulated baryon circular velocity profiles (blue dashed lines in Fig. 11). The baryon

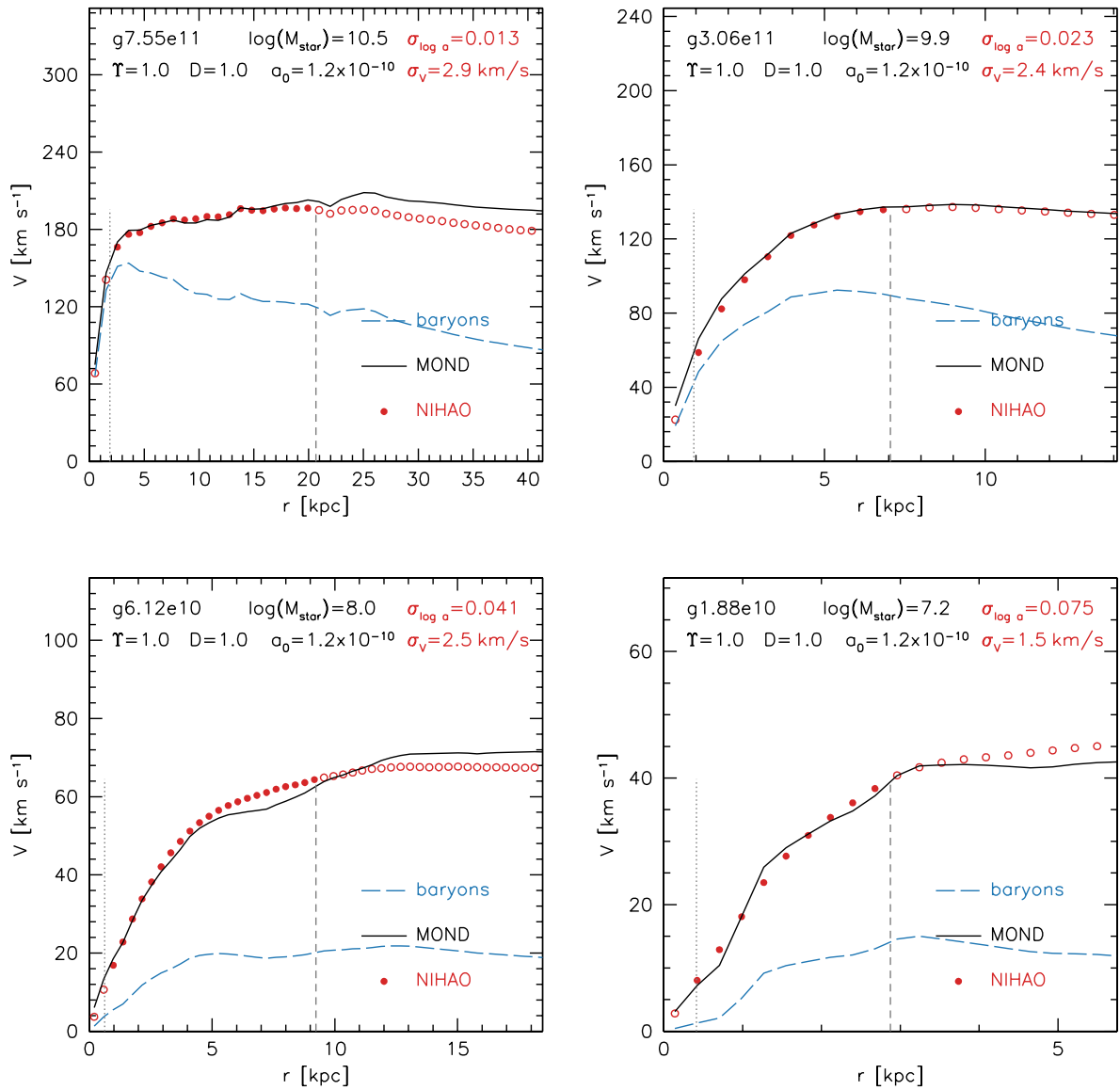


**Figure 11.** Examples of NIHAO circular velocity curves (red circles) where the MOND prediction (black lines) works well. The vertical grey lines show twice the dark matter softening length (dotted) and the HI radius (dashed). The standard deviation of the velocity residuals,  $\sigma_V$ , and acceleration residuals,  $\sigma_{\log a}$ , is computed for data points between these two lines and is given in the top right corner of each panel. These galaxies span over three orders of magnitude in stellar masses.

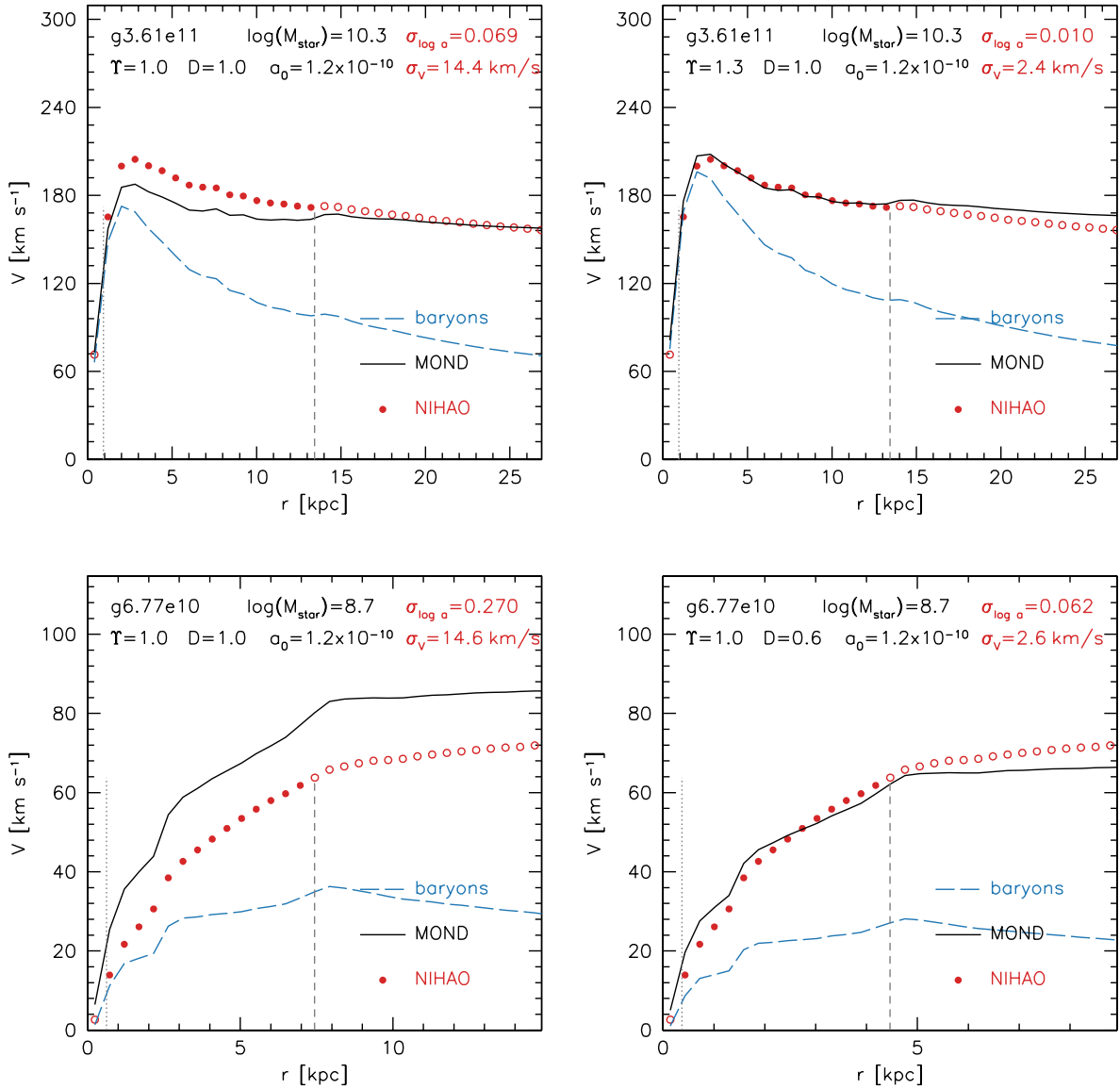
circular velocity profiles are the (quadratic) sum of the circular velocity due to the stars and gas, calculated from the gravitational potential in the plane of the disk.

Fig. 11 shows examples of four simulations for which the MOND prescription (fitted to the SPARC data) accurately predicts the circular velocity profile of the simulation. The standard deviation of  $V$  and  $\log a$  is given in the top right corner. The agreement, to within  $3 \text{ km s}^{-1}$ , is remarkable! We stress that there are no free parameters. The stellar masses of these examples range over more than three orders of magnitude from  $10^{7.2}$  to  $10^{10.5} M_{\odot}$ .

However, we have chosen these 4 examples out of a sample of 89 examples. Fig. 12 shows examples of two simulations for which the MOND prescription clearly fails, one

where MOND under-predicts the velocity ( $g3.61e11$ , upper left) and another where MOND over-predicts ( $g6.77e10$ , lower left). For  $g3.61e11$  an excellent fit can be obtained simply by rescaling the stellar mass profile by a factor of 1.3 (i.e., 0.11 dex), which is a typical uncertainty on an observed stellar mass-to-light ratio. For  $g6.77e10$  changing the stellar mass normalization has little impact because the baryons are dominated by gas. In this case a good fit can be obtained by reducing the distance by 40%. This would be a  $2\sigma$  uncertainty in distances. One can also change the acceleration scale,  $a_0$ , to obtain a similar effect.

Fig. 13 shows the standard deviation of MOND fits to NIHAO circular velocity profiles. The fiducial (no free parameter) fit is shown with red open circles. The median error



**Figure 12.** Examples of NIHAO circular velocity curves where MOND fails. Top left: MOND under predicts the velocity. An excellent fit can be obtained by increasing the stellar mass by 30% (top right), mimicking the observational uncertainty in the stellar mass-to-light ratio. Bottom left: MOND over predicts the velocity. A good fit can be obtained by reducing the distance by 40% (bottom right).

is just  $6 \text{ km s}^{-1}$ . If we allow the stellar mass and distance to vary, we can obtain even better fits (black circles), with a median error of just  $2.5 \text{ km s}^{-1}$ . This analysis is of relevance to the study of Li et al. (2018) who are able to fit the SPARC sample with a single RAR, allowing for variation in  $M/L$  of the disk and bulge, distance and inclination. At first this seems an impressive result for MOND. However, our similar analysis of NIHAO galaxies shows that MOND fits have too much freedom, and can fit galaxy velocity profiles that they should not be able to.

These figures also highlight some of the issues with measuring the scatter in the RAR. Because the scatter is measured in logarithmic space, galaxies with flat rotation curves tend to have smaller scatter than those with rising rotation curves where errors at small velocities get magnified. The

other issue is spatial sampling. Here we sample galaxies uniformly in units of the virial radius, but we only include points that are observable (i.e., within the HI radius). Thus for two galaxies that live in similar mass haloes but have different HI sizes, the larger galaxy will have more points in the RAR. This implies that galaxies effectively have different weights in the RAR. Given the current large uncertainties in the intrinsic scatter this is a detail, but in the future it will be necessary to sample the rotation curves in observations and theory in a consistent way (see e.g., Desmond 2017).

## 5.1 Dark matter profiles

Since the RAR is a prescription of predicting the total acceleration given the baryon acceleration, it is thus a pre-

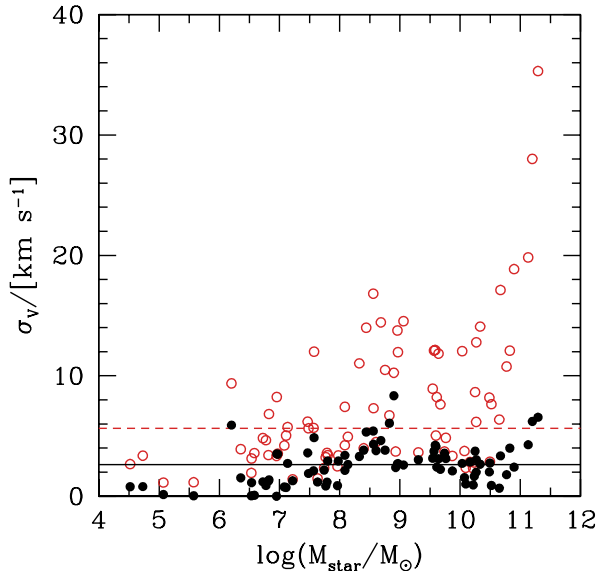


**Figure 13.** Residuals of MOND fits to NIHAO circular velocity curves. Fiducial fits (red open circles) which have no free parameters, result in a median scatter of just 6 km/s. When the stellar mass and “distance” are fitted for (black filled circles) residuals are reduced even further to 2.5 km/s.

scription for predicting the mass discrepancy or in other words the dark matter acceleration. When the RAR works well in NIHAO this means that RAR is accurately predicting the dark matter profile. By construction, for the galaxies where the RAR under-predicts the circular velocity, the RAR under-predicts the dark matter halo, and for the galaxies where the RAR over-predicts the circular velocity, RAR over-predicts the dark matter halo. It is then interesting to compare the dark matter profiles from the RAR with those from the NIHAO and DMO simulations. This comparison is made in Fig. 14.

Each panel shows a different stellar mass range (corresponding to those used in Figs. 7 - 9), except we have split the highest mass bin into two to make clearer the different dark matter profiles at the highest masses we simulate. The mean  $\log(M_{\text{star}})$  is indicated in the top left of each panel. The thick lines show mean (of  $\log V$ ) dark matter circular velocity profiles for NIHAO (red solid), DMO (cyan long dashed) and NIHAO MOND (black short-dashed). The thin lines show the standard deviation (of  $\log V$ ).

One of the striking differences between  $\Lambda$ CDM (both DMO and NIHAO) and MOND is that at large radii (i.e., close to the virial radius) MOND always over-predicts the circular velocity. This is because of the assumption that  $a^2 \propto a_{\text{bar}}$  at low accelerations. If all the baryons were near the center of the halo, the velocity profile would indeed become flat (which would not be as bad, but still not in agreement with the declining velocity profiles of the simulations), but it rises at large radii due to the gas in the halo. Recall that in our comparison to SPARC data we only considered radii that can be traced with atomic hydrogen gas, which typically only extends up to 5-10% of the virial radius (see the red circles in Fig. 14 which show the average HI radius). Restricting to the

observable radii, the MOND dark matter profiles typically fall between the DMO and NIHAO lines.

At stellar masses between  $10^7 \lesssim M_{\text{star}} \lesssim 10^{10} M_{\odot}$  the NIHAO simulations have resulted in halo expansion to a constant density (compare with the reference lines for  $\rho \propto r^{-\alpha}$  with  $\alpha = 0$  and  $\alpha = 1$ ), see also Tollet et al. (2016). MOND also tends to predict expanded haloes, but not as much as in NIHAO.

For the highest masses ( $M_{\text{star}} = 10^{10.9} M_{\odot}$ , top left panel) the NIHAO simulations have contracted dark haloes, while MOND predicts expansion. These are examples similar to that shown in the top left of Fig. 12, where this deficit in dark matter can be compensated for with increased stellar mass. In spite of these differences, because the centers of these galaxies are dominated by baryons, they are only offset by a small amount from the SPARC RAR. The average rms in  $a$  of these 8 galaxies is 0.056 dex, making them typical galaxies. Determining the dark matter profiles observationally, and thus distinguishing between the predictions from MOND and NIHAO requires an accurate determination of the stellar mass-to-light ratio, which is a challenge.

A summary of the density profiles is shown in Fig. 15. This shows the dark matter circular velocity at 1% of the virial radius vs stellar mass (left panel) and the slope of the dark matter circular velocity between 1 and 2% of the virial radius [ $\gamma_V = \log_{10}(V_{0.02}/V_{0.01})/\log_{10}(2)$ ] vs stellar mass (right panel). Both plots show the same qualitative trends. DMO simulations (cyan) have structure that is almost scale free, with velocity  $\log_{10}[V_{\text{dark}}(0.01R_{200})/V_{200}] \simeq -0.25$  and velocity slope  $\gamma_V \simeq 0.5$ . Note that we choose to show velocity slope rather than (local) density slope because the latter involves an extra derivative of the velocity profile, and so is noisier in both observations and simulations. The circular velocity profile, or equivalently the cumulative mass profile, or cumulative enclosed mass density profile, also has advantages in terms of analytic models (Dekel et al. 2017). The velocity slope can be easily converted into an enclosed mass density slope using  $\gamma_{\rho} = 2\gamma_V - 2$ . So for example a constant density core,  $\gamma_{\rho} = 0$  corresponds to a velocity slope of  $\gamma_V = 1$ , a NFW density slope of  $\gamma_{\rho} = -1$  corresponds to a velocity slope of  $\gamma_V = 0.5$ , and an isothermal density slope of  $\gamma_{\rho} = -2$  corresponds to a velocity slope of  $\gamma_V = 0$ .

In NIHAO hydro simulations (red points and lines) the halo response is strongly mass dependent (See also Tollet et al. 2016; Dutton et al. 2016). At low stellar masses  $M_{\text{star}} \lesssim 10^6 M_{\odot}$  there is very little halo response. As the stellar mass increases the halo expands (i.e., lower velocity and higher velocity slope), reaching a maximum expansion at stellar masses of  $M_{\text{star}} \sim 10^9 M_{\odot}$ , where the velocities are  $\simeq 0.4$  dex lower and the velocity slopes are 0.4 higher than DMO and close to a constant density core ( $\gamma_V = 1$ ). By a mass of  $M_{\text{star}} \sim 10^{10.5} M_{\odot}$  the haloes are on average unchanged at small radii, and at the highest stellar masses  $M_{\text{star}} \sim 10^{11} M_{\odot}$  the haloes contract at small radii. The MOND dark matter haloes (black points and lines) typically show behavior intermediate between NIHAO and DMO (i.e., the haloes are not as cuspy and DMO, and not as expanded as NIHAO). The exception is at the highest masses, where MOND haloes have lower velocities and higher slopes, the opposite of NIHAO, which has higher velocities and lower slopes.

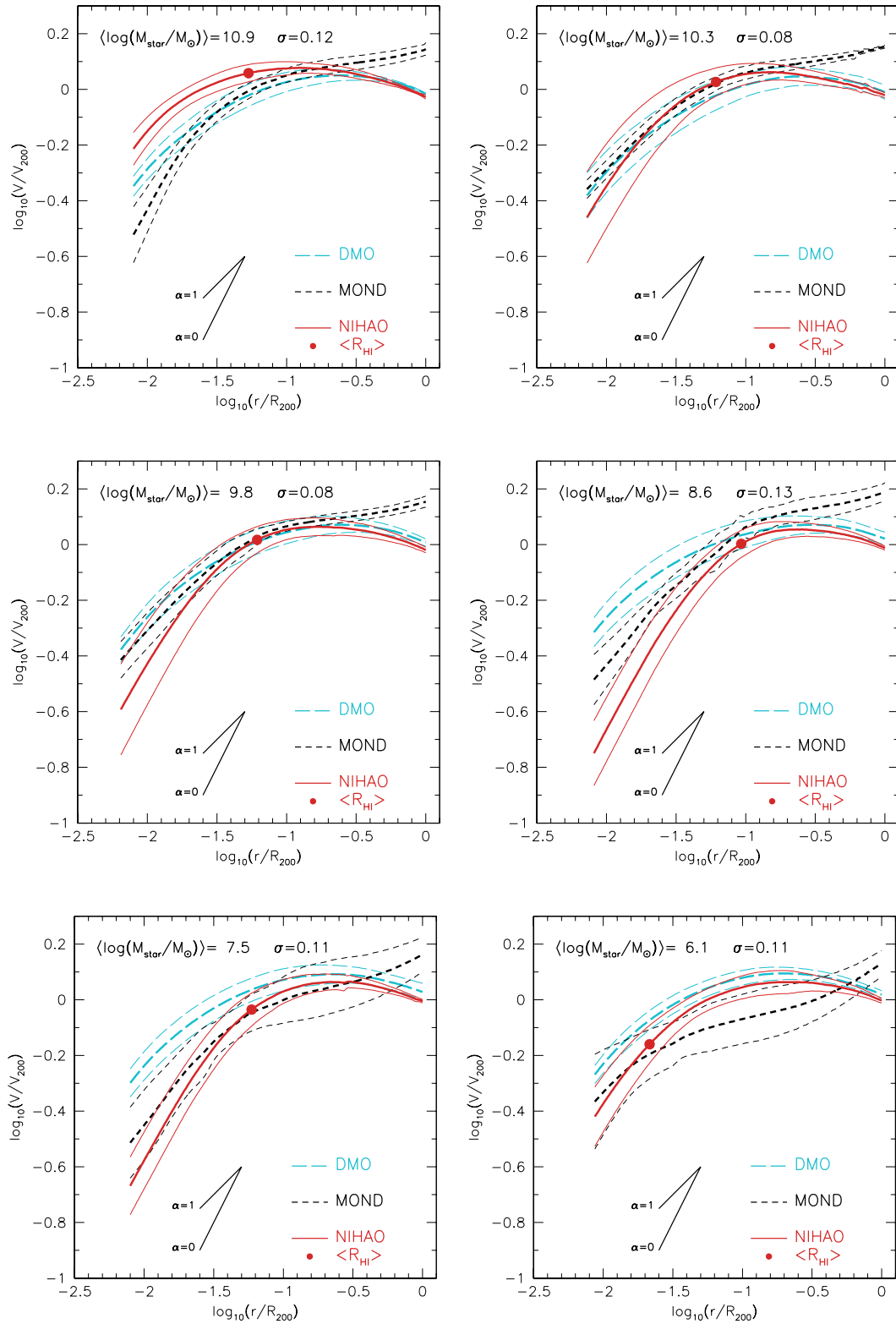


**Figure 14.** Dark matter circular velocity profiles from simulations. Dark matter only simulation (long-dashed cyan), hydrodynamical (red solid), and MOND prediction using the baryon circular velocity from the hydrodynamical simulation (short-dashed black). Lines are plotted between twice the dark matter softening to the virial radius. The red dot shows the average HI radius (enclosing 90% of the HI mass). Each panel shows galaxies with a different range of stellar mass, the average stellar mass  $\langle \log_{10}(M_{\text{star}}/M_{\odot}) \rangle$  is indicated in the top left of each panel. The standard deviation between the NIHAO and MOND dark matter velocity profiles is given by  $\sigma$ . For reference we show lines with density slopes  $\alpha = 0$  and  $\alpha = 1$ , where  $\rho \propto r^{-\alpha}$ . One can see systematic deviations between MOND and hydro simulations.

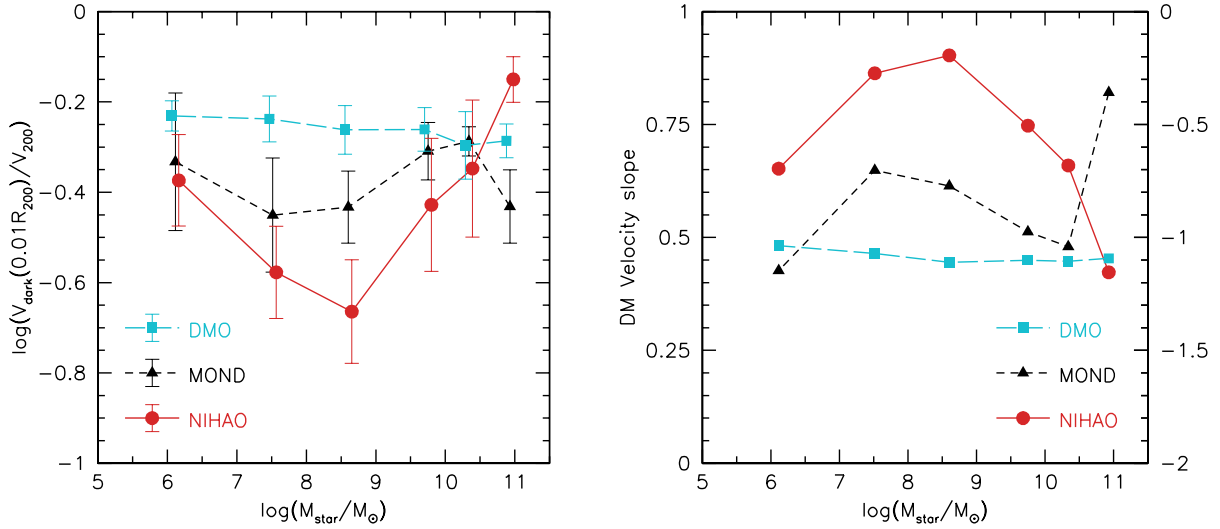


**Figure 15.** Dark matter circular velocity at 1% of the virial radius (left) and dark matter circular velocity slope between 1-2% of the virial radius (right) for NIHAO hydro (red solid), DMO (cyan long-dashed), and MOND (black short-dashed). The right axis of the right panel shows the enclosed DM density slope. Stellar mass bins are the six panels shown in Fig. 14. DMO simulations have a velocity and velocity slope independent of the stellar mass. NIHAO hydro simulations have contraction at the highest stellar masses, and maximum expansion for stellar masses of  $M_{\text{star}} \sim 10^9 M_{\odot}$ . MOND haloes are typically intermediate between DMO and Hydro, except for the highest stellar mass, where MOND predicts expansion to a core while NIHAO predicts a contracted cusp.

## 6 SUMMARY

We use 89 cosmological galaxy formation simulations from the NIHAO project (Wang et al. 2015) to study the origin of the radial acceleration relation (RAR) in a  $\Lambda$ CDM universe. The unique combination of halo mass range, resolution, and number of haloes allows us to compare with observations of the RAR from the SPARC survey (McGaugh et al. 2016). The NIHAO galaxies have stellar masses spanning  $10^{4.5} \lesssim M_{\text{star}} \lesssim 10^{11.3} M_{\odot}$ .

We summarize our results as follows:

- The RAR exists in the NIHAO simulations with a similar slope and normalization as observationally determined by SPARC (Fig. 4).
- The RAR in NIHAO has a scatter of 0.079 dex. This is consistent with estimates of the intrinsic scatter from observations ( $0.0 \lesssim \sigma_{\text{int}} \lesssim 0.09$ ) (Fig. 5).
- The scatter in the RAR depends on the stellar mass of the galaxy, with lower scatter in higher mass galaxies in both observations and simulations (Fig. 6). For high mass galaxies ( $M_{\text{star}} \gtrsim 10^{9.3} M_{\odot}$ ) the intrinsic scatter ( $\sigma_{\text{int}} \lesssim 0.05$ ) is consistent with both MOND and NIHAO. However, for low mass galaxies ( $M_{\text{star}} \lesssim 10^{9.3} M_{\odot}$ ) the intrinsic scatter ( $0.10 \lesssim \sigma_{\text{int}} \lesssim 0.15$ ) is consistent with NIHAO, but inconsistent with MOND.
- The mass dependence of the RAR scatter in simulations is partially explained by the correlation between  $a \equiv a_{\text{bar}} + a_{\text{dm}}$  and  $a_{\text{bar}}$  at low dark matter fractions.
- In the lowest mass galaxies we simulate ( $M_{\text{star}} \sim 10^6 M_{\odot}$ ) The RAR deviates significantly from the MOND prediction, but is in agreement with the observed RAR from dwarf spheroidal galaxies (Fig. 9).
- We can use the RAR to accurately predict (to within

a few  $\text{km s}^{-1}$ ) the circular velocity profiles of individual NIHAO simulations by just using the baryon circular velocity profile as input (Fig. 11).

- In cases where the fiducial values provide a bad fit, the stellar masses can be re-scaled, and/or the distances changed to provide excellent fits (Fig. 12). Given realistic uncertainties in baryon profiles and galaxy distances, MOND has too much flexibility in fitting individual galaxy rotation curves. Thus the success of MOND at fitting individual galaxy rotation curves is not as impressive as it is often claimed to be (e.g., Sanders & McGaugh 2002; Li et al. 2018).

- The RAR predicts dark matter circular velocity profiles that are on average similar to that found in  $\Lambda$ CDM simulations (Fig. 14).

- In detail, the RAR generally predicts mild halo expansion at small radii (relative to dissipationless CDM), but not as much expansion as found in the NIHAO simulations (Fig. 15). This contradicts the claim by Navarro et al. (2017) that explaining the RAR in CDM does not require modifications to the cuspy inner mass profiles of dark haloes.

- The largest differences in the dark matter profiles are in the highest mass galaxies we simulate. For ( $M_{\text{star}} \sim 10^{11} M_{\odot}$ ) NIHAO predicts halo contraction, while the RAR predicts expansion to a dark matter core (Figs. 14 & 15).

It may seem paradoxical that the MOND RAR appears to be in the NIHAO  $\Lambda$ CDM galaxy formation simulations. The resolution is both MOND and NIHAO are approximating the same thing (the observable Universe).

Since the phenomenological basis for MOND is naturally reproduced by  $\Lambda$ CDM galaxy formation simulations, it seems unnecessary to invoke the simplifying assumptions and radical new force law required by MOND. A useful analogy is with solar system. A phenomenological theory might

assume that the orbits of planets are circles, since they are observed to be roughly circles, and this is the simplest geometry. But we know that with sufficiently accurate observations the orbits are actually ellipses, and the circle model is an over-simplification.

The assumptions MOND is based on are only approximately true in  $\Lambda$ CDM: 1) At high accelerations the dark matter fraction is low, but non-zero; 2) Circular velocity profiles are only approximately flat at the HI radius of a galaxy. At larger radii the profiles decline; 3) The scatter in the RAR is small, but non-zero, primarily reflecting non-universality of the dark matter density profiles. Finally, we note that if one wishes to go beyond Newtonian dynamics there is more freedom in the observed RAR than imposed by MOND.

## ACKNOWLEDGMENTS

We thank the referee for a prompt report that led to significant improvements in the paper. The authors gratefully acknowledge the Gauss Centre for Supercomputing e.V. ([www.gauss-centre.eu](http://www.gauss-centre.eu)) for funding this project by providing computing time on the GCS Supercomputer SuperMUC at Leibniz Supercomputing Centre ([www.lrz.de](http://www.lrz.de)). Part of this research was also carried out on the High Performance Computing resources at New York University Abu Dhabi; on the THEO cluster of the Max-Planck-Institut für Astronomie; and on the HYDRA cluster at the Rechenzentrum in Garching. We greatly appreciate the contributions of all these computing allocations. AO is funded by the Deutsche Forschungsgemeinschaft (DFG, German Research Foundation) – MO 2979/1-1. TB was supported by the Sonderforschungsbereich SFB 881 “The Milky Way System” (sub-projects A1 and A2) of the DFG. The analysis made use of the PYNBODY package ([Pontzen et al. 2013](#)).

## REFERENCES

- Bond, J. R., Efstathiou, G., & Silk, J. 1980, *Physical Review Letters*, 45, 1980
- Buck, T., Macciò, A. V., Obreja, A., et al. 2017, *MNRAS*, 468, 3628
- Courteau, S., Dutton, A. A., van den Bosch, F. C., MacArthur, L. A., Dekel, A., McIntosh, D. H., & Dale, D. A. 2007, *ApJ*, 671, 203
- Dekel, A., Ishai, G., Dutton, A. A., & Macciò, A. V. 2017, *MNRAS*, 468, 1005
- Desmond, H. 2017, *MNRAS*, 464, 4160
- Di Cintio, A., & Lelli, F. 2016, *MNRAS*, 456, L127
- Dutton, A. A., & Macciò, A. V. 2014, *MNRAS*, 441, 3359
- Dutton, A. A., Macciò, A. V., Frings, J., et al. 2016a, *MNRAS*, 457, L74
- Dutton, A. A., Obreja, A., Wang, L., et al. 2017, *MNRAS*, 467, 4937
- Dutton, A. A., Obreja, A., & Macciò, A. V. 2019, *MNRAS*, 482, 5606
- Faber, S. M., & Gallagher, J. S. 1979, *ARA&A*, 17, 135
- Gill, S. P. D., Knebe, A., & Gibson, B. K. 2004, *MNRAS*, 351, 399
- Gutcke, T. A., Stinson, G. S., Macciò, A. V., Wang, L., & Dutton, A. A. 2017, *MNRAS*, 464, 2796
- Keller, B. W., & Wadsley, J. W. 2017, *ApJ*, 835, L17
- Knollmann, S. R., & Knebe, A. 2009, *ApJS*, 182, 608

- Kravtsov, A. V. 2013, *ApJ*, 764, L31
- Lelli, F., McGaugh, S. S., & Schombert, J. M. 2016, *AJ*, 152, 157
- Lelli, F., McGaugh, S. S., Schombert, J. M., & Pawlowski, M. S. 2017, *ApJ*, 836, 152
- Li, P., Lelli, F., McGaugh, S., & Schombert, J. 2018, *A&A*, 615, A3
- Ludlow, A. D., Benítez-Llambay, A., Schaller, M., et al. 2017, *Physical Review Letters*, 118, 161103
- Macciò, A. V., Udrescu, S. M., Dutton, A. A., et al. 2016, *MNRAS*, 463, L69
- McGaugh, S. S. 2004, *ApJ*, 609, 652
- McGaugh, S. S., & Schombert, J. M. 2015, *ApJ*, 802, 18
- McGaugh, S. S., Lelli, F., & Schombert, J. M. 2016, *Physical Review Letters*, 117, 201101
- Milgrom, M. 1983, *ApJ*, 270, 365
- Navarro, J. F., Benítez-Llambay, A., Fattahi, A., et al. 2017, *MNRAS*, 471, 1841
- Planck Collaboration, Ade, P. A. R., Aghanim, N., et al. 2014, *A&A*, 571, A16
- Pontzen, A., Roškar, R., Stinson, G., & Woods, R. 2013, *Astrophysics Source Code Library*, 1305.002
- Rahmati, A., Schaye, J., Pawlik, A. H., & Raičević, M. 2013, *MNRAS*, 431, 2261
- Rodrigues, D. C., Marra, V., del Popolo, A., & Davari, Z. 2018, *Nature Astronomy*, 2, 668
- Sanders, R. H. 1990, *A&ARv*, 2, 1
- Sanders, R. H., & McGaugh, S. S. 2002, *ARA&A*, 40, 263
- Santos-Santos, I. M., Di Cintio, A., Brook, C. B., et al. 2018, *MNRAS*, 473, 4392
- Smoot, G. F., Bennett, C. L., Kogut, A., et al. 1992, *ApJ*, 396, L1
- Stinson, G., Seth, A., Katz, N., et al. 2006, *MNRAS*, 373, 1074
- Stinson, G. S., Brook, C., Macciò, A. V., et al. 2013, *MNRAS*, 428, 129
- Stinson, G. S., Dutton, A. A., Wang, L., et al. 2015, *MNRAS*, 454, 1105
- Tollet, E., Macciò, A. V., Dutton, A. A., et al. 2016, *MNRAS*, 456, 3542
- van den Bosch, F. C., & Dalcanton, J. J. 2000, *ApJ*, 534, 146
- Wadsley, J. W., Keller, B. W., & Quinn, T. R. 2017, *MNRAS*, 471, 2357
- Wang, L., Dutton, A. A., Stinson, G. S., Macciò, A. V., Penzo, C., Kang, X., Keller, B. W., Wadsley, J. 2015, *MNRAS*, 454, 83
- Zwicky, F. 1933, *Helvetica Physica Acta*, 6, 110

This paper has been typeset from a  $\text{\TeX}/\text{\LaTeX}$  file prepared by the author.